3-1-2013

Faraday Rotation Distributions from Stellar Magnetism in Wind-Blown Bubbles.

Richard Ignace
East Tennessee State University

N. Pingel
University of Wisconsin-Madison

Citation Information

Ignace, Richard; and Pingel, N.. 2013. Faraday Rotation Distributions from Stellar Magnetism in Wind-Blown Bubbles.. *The Astrophysical Journal*. Vol.765 https://doi.org/10.1088/0004-637X/765/1/19 ISSN: 0004-637X

Faraday Rotation Distributions from Stellar Magnetism in Wind-Blown Bubbles.

The Astrophysical Journal, 765:19 (10pp), 2013 March 1 doi:10.1088/0004-637X/765/1/19

FARADAY ROTATION DISTRIBUTIONS FROM STELLAR MAGNETISM IN WIND-BLOWN BUBBLES

R. Ignace[1] and N. M. Pingel[2]
[1] Department of Physics and Astronomy, East Tennessee State University, Johnson City, TN 37614, USA; ignace@etsu.edu
[2] Department of Astronomy, University of Wisconsin-Madison, Madison, WI 53711, USA; nmpingle@wisc.edu
Received 2012 October 29; accepted 2013 January 4; published 2013 February 13

ABSTRACT

Faraday rotation is a valuable tool for detecting magnetic fields. Here, the technique is considered in relation to wind-blown bubbles. In the context of spherical winds with azimuthal or split monopole stellar magnetic field geometries, we derive maps of the distribution of position angle (P.A.) rotation of linearly polarized radiation across projected bubbles. We show that the morphology of maps for split monopole fields are distinct from those produced by the toroidal field topology; however, the toroidal case is the one most likely to be detectable because of its slower decline in field strength with distance from the star. We also consider the important case of a bubble with a spherical sub-volume that is field-free to approximate crudely a "swept-up" wind interaction between a fast wind (or possibly a supernova ejecta shell) overtaking a slower magnetized wind from a prior state of stellar evolution. With an azimuthal field, the resultant P.A. map displays two arc-like features of opposite rotation measure, similar to observations of the supernova remnant G296.5+10.0. We illustrate how P.A. maps can be used to disentangle Faraday rotation contributions made by the interstellar medium versus the bubble. Although our models involve simplifying assumptions, their consideration leads to a number of general robust conclusions for use in the analysis of radio mapping data sets.

Key words: circumstellar matter – ISM: supernova remnants – polarization – radio continuum: stars – stars: magnetic field – stars: winds, outflows

Online-only material: color figures

1. INTRODUCTION

Magnetism plays an important role in the lives of stars, frequently in the form of its influence on angular momentum transport for star formation and evolution (e.g., Ghosh & Lamb 1979; Blandford & Payne 1982; Bodenheimer 1995; McKee & Ostriker 2007; Meynet et al. 2011; Matt et al. 2012), and also in terms of hot plasma generation (e.g., Davidson & Ostriker 1973; Babel & Montmerle 1997a, 1997b; Townsend et al. 2007; Li et al. 2008; Güdel & Nazé 2009). Of interest to this paper is the growing body of evidence for magnetism among massive stars. Direct detections of magnetism in normal stars (i.e., not compact objects) are in large part relegated to measuring circular polarizations in spectral lines arising from the Zeeman effect (see Donati & Landstreet 2009). The first detection of magnetism in a star besides the Sun dates back to Babcock (1947). Since then, the field has exploded. A recent review of the current state of the subject for non-degenerate stars can be found in Donati & Landstreet (2009). The key result now is that whereas magnetic detections were mainly limited to stars with surface fields in the kilogauss range, modern instrumentation and diagnostic strategies regularly achieve highly significant detections in the regime of hundreds of gauss (e.g., Donati & Collier Cameron 1997), and in some special cases much less (e.g., Sennhauser & Berdyugina 2011).

Numerous direct detections of surface magnetism in massive stars have been reported, with some recent examples being Alecian et al. (2011), Petit et al. (2011), Schöller et al. (2011), Hubrig et al. (2011, 2012) Grunhut et al. (2012a, 2012b, 2013), and Wade et al. (2011, 2012). These successes have correspondingly motivated theoretical studies to understand the origin of these fields for massive stars (e.g., MacGregor & Cassinelli 2003; Braithwaite 2006; Cantiello et al. 2009), their influence on massive star evolution (Maeder & Meynet 2003; Yoon et al. 2012), and connection to other observational phenomena such as X-ray emissions (Babel & Montmerle 1997b; Gagne et al. 1997, 2005; Favata et al. 2009; Ignace et al. 2010, 2013; Oskinova et al. 2011; Gagne et al. 2011; Wade et al. 2012; Grunhut et al. 2013) and aspherical wind flow (Poe et al. 1989; Shore & Brown 1990; Chevalier & Luo 1994; ud-Doula & Owocki 2002; Townsend & Owocki 2005; Brown et al. 2008; ud-Doula et al. 2008, 2013).

There are other diagnostics of stellar magnetism that have or could complement the Zeeman-based approach. Non-thermal radio emissions from massive star colliding wind binaries have been used to infer stellar magnetism (e.g., Williams et al. 1997; Dougherty & Williams 2000; De Becker et al. 2006; van Loon et al. 2006). The Hanle effect is a weak Zeeman effect pertaining to the influence of magnetic fields on the linear polarization in spectral lines. The effect is sensitive to magnetic fields in the 1–100 G range (depending on the Einstein A-value of the lines being measured) and has been successfully used in studies of solar magnetism for decades (e.g., Sahal-Brechot et al. 1977; Stenflo 1982; Berdyugina & Fluri 2004; Trujillo Bueno et al. 2005). There is a small but growing literature on its potential application to other stars (Ignace et al. 1997, 2011; Lopez Ariste et al. 2011; Bommier 2012; Manso Sainz & Martinez Gonzalez 2012).

Another important method for measuring astrophysical magnetic fields is Faraday rotation. The effect refers to how the line-of-sight (LOS) magnetic field component rotates the position angle (P.A.) of linear polarization for a beam of radiation. The amount of rotation is also proportional both to the electron density (hence operates only in a plasma) and to the path length through such regions. Importantly, the amount of P.A. rotation scales with the square of the wavelength of observation, λ^2. In this way most applications measure the polarization P.A. for a range of wavelengths to derive a quantity called the "rotation

measure" (or RM; see the following section) that encodes information about the integrated product of the LOS field component and electron number density.

Most applications of Faraday rotation are for interstellar or extragalactic studies. Space precludes a comprehensive review of this literature; discussion of the state of the field, with references therein, can be found, for example, in Carilli & Taylor (2002), Han et al. (2006), and Beck (2012). Here attention is focused on the potential of Faraday rotation as a probe of stellar magnetism in wind-blown bubbles. There has been several recent observational developments that speak to the interaction of stellar winds or supernova explosions with the surrounding interstellar environment and the capacity of probing these interactions with Faraday rotation.

Ransom et al. (2008, 2010) have conducted studies of Faraday rotation effects arising from planetary nebulae (PNe). The relative motion between a PN and the surrounding interstellar medium (ISM) alters the strength and direction of the interstellar magnetic field, leading to variations of the polarization P.A. across the PNe and the trailing tail it creates in relation to the P.A.s surrounding the structure. Although implicitly placing constraints on the stellar magnetic field interior to the nebula, the PNe act essentially as perturbers, on the scale of a few parsecs, of the local medium, with Faraday rotation serving as a probe of the resultant disturbances.

Regarding massive star influences, Savage et al. (2012) report on an extensive study of Faraday rotation for the HII region, the Rosette Nebula. In this application, a cluster of massive stars lead to a wind-blown bubble and surrounding photoionized region by the central OB stars. In contrast to the PN studies of Ransom et al. (2008, 2010), whose analysis was based on P.A. maps with the diffuse Galactic synchrotron used as a source of linearly polarized radiation, the Rosette study of Savage et al. analyzed data from an array of sight lines to background extragalactic sources of polarized emission that intercept the nebula and surrounding region. Their data are consistent with P.A. changes across the nebula, on a scale of $\sim$10 pc, arising from the presence of the bubble and its impact on the interstellar magnetic field.

For the case of Faraday rotation as a probe of stellar magnetism, Harvey-Smith et al. (2010) discuss an antisymmetric RM morphology across the supernova remnant (SNR) G296.5+10.0. The SNR nebula has two prominent emission arcs on opposite sides of a symmetry axis, yet the P.A. rotations of either arc are oppositely oriented. This kind of pattern would be expected from a magnetic field that reverses its LOS polarity from one arc to the other. The authors associated the pattern with the magnetic field of a slow magnetized red supergiant wind. The ejecta shell from the SN has "swept up" the supergiant wind into the observed shell. To reproduce the RM pattern, the stellar magnetic field would have to be toroidal to produce the observed polarity change between the emission arcs. The authors derive an expression to relate the observed scale of P.A. rotations to properties of the shell and the stellar wind. The observed change in amplitude of the RM by approximately 40 rad m^{-2} indicates that a surface stellar magnetic field on the order of 500 G could account for the observations.

In this paper, we explore further the idea of Faraday rotation as a means of deriving information about stellar magnetism in the large-scale wind that might sometimes be observed in wind-blown bubbles and SNRs. In Section 2, a brief review of the expressions describing Faraday rotation are given. A derivation of P.A. rotation maps for an ionized and spherical stellar wind with azimuthal (or toroidal) magnetic fields is presented in Section 2.1. P.A. rotation maps for a split monopole are presented in Section 2.2 as a contrast case. Returning to the azimuthal field in Section 2.3, simple insertion of a spherical sub-volume taken to have no magnetic field is used to simulate a two-wind interaction like that of a SNR or any scenario in which a fast flow overtakes a slower one from an earlier stage of stellar evolution. In Section 3 applications of our results are discussed, with concluding remarks given in Section 4.

2. THEORETICAL MODELS

The standard expression to represent the polarization P.A. rotation, ψ, arising from Faraday rotation along a sight line is

$$\psi = \psi_0 + \mathrm{RM} \times \left(\frac{\lambda}{1\,\mathrm{m}}\right)^2, \tag{1}$$

where ψ_0 is the orientation of a background polarization upon which Faraday rotation operates, and RM is the "rotation measure" given by the path length integral of

$$\mathrm{RM} = 0.81\,\mathrm{rad\,m^{-2}} \int \left(\frac{B_\parallel}{\mu\mathrm{G}}\right)\left(\frac{n_\mathrm{e}}{\mathrm{cm^{-3}}}\right)\left(\frac{dz}{\mathrm{pc}}\right), \tag{2}$$

where $B_\parallel$ is the LOS component of the magnetic field, n_e is the electron density, and path length.

The rationale for this particular formulation is that observers are frequently interested in deriving RM from the radio data as a constraint on the magnetic field strength (modulo the electron density, whose value may be constrained from other considerations). One measures values of ψ for a range of wavelengths; plotting ψ against λ^2 in a log–log plot should then yield a straight line whose slope is the rotation measure, RM. If RM $>$ 0, then the net Faraday rotation from all of the parallel field components along the LOS, some being positive and some being negative, in regions where there are electrons has resulted in a counterclockwise rotation of the background linearly polarized radiation. If RM $<$ 0, the net effect is a clockwise rotation. The sign of ψ, or alternatively RM, is sensitive to the electron-density averaged net LOS field component along a given sight line.

The distinction being drawn here is that our models emphasize *differential* Faraday rotation (e.g., Minter & Spangler 1996). This amounts to a map of how RM varies between neighboring sight lines, which is equivalent to analyzing maps of ψ at a fixed wavelength. Consequently, it is convenient for our purposes to reformulate the effect of Faraday rotation as

$$\psi = \frac{\pi}{z_0(\lambda)} \int \left(\frac{B_\parallel}{B_0}\right)\left(\frac{n_\mathrm{e}}{n_0}\right) dz, \tag{3}$$

where n_0 and B_0 are chosen normalizations, $z_0(\lambda)$ is a relevant length scale for the problem, dz is in the same units of z_0, and the factor of π is made explicit here both to indicate that ψ is measured in radians and to highlight the fact that polarization P.A. is degenerate in multiples of π (or 180°).

It is straightforward to convert such a map in P.A. to one in RM. If one evaluates $\psi(\lambda_0)$ at a reference wavelength λ_0, then

$$\psi(\lambda) = \psi(\lambda_0) \times \frac{\lambda^2}{\lambda_0^2}, \tag{4}$$

and so

$$\mathrm{RM} = \frac{\psi(\lambda_0)}{\lambda_0^2}. \tag{5}$$

The following discussion of Faraday rotation in stellar bubbles adopts the use of Equation (3).

We focus on three illustrative cases to highlight expected P.A. map morphologies as motivated by current observations. First the case of an azimuthal field distribution is considered. Since the field strength diminishes only as r^{-1}, it is this component that is most likely to have observational relevance at the 1–10 pc scales of stellar bubbles. Second, as a contrast case, P.A. maps are derived for a split monopole field. This case leads to results that are morphologically distinct from the azimuthal field case. The field drops much faster with distance from the star, as r^{-2}, making this case essentially unobservable; still, the split monopole has value in providing insight into the range of morphological possibilities. Finally, we consider again the azimuthal field scenario but now imposing a central "cavity" that does not contribute to Faraday rotation (e.g., a central region devoid of a magnetic field). This approximates a "swept-up" field from a wind–wind interaction, such as may occur for an SNR or a PN, where only the wind from an earlier phase of stellar evolution has a relevant magnetic field.

We stress that spherical symmetry is adopted for the bubble shape and density distribution. It is not the goal of this paper to reproduce the observations for any particular object. A spherically symmetric density profile provides a "controlled" environment for which to evaluate and gain insight into Faraday rotation through stellar bubbles. Real situations may involve a broad range of additional (and potentially important) considerations, such as aspherical density distributions (e.g., bipolar flows or clumping); radius-dependent and/or aspherical ionization effects; correlated behavior between density, ionization, and/or a dynamically relevant magnetic field (e.g., how a toroidal field can lead to axisymmetric bubbles as described in Chevalier & Luo 1994). Our spherical results provide a suite of baseline cases that are analytic or semianalytic in which one can evaluate modifications to predicted P.A. maps arising from these more complex factors.

Before proceeding it is useful first to review the different contributing components to Faraday rotation that affect the final observed P.A. at Earth. The underlying assumption is that Faraday rotation acts to rotate the P.A. of linearly polarized radiation as it passes through magnetized and ionized regions. The background source (whether a point source or diffuse synchrotron background) has some initial position angle $\psi_{\rm orig}$. This value receives an additional contribution $\psi_{\rm ISM}$ owing to the ISM. The total P.A. measured at Earth is then

$$\psi_{\rm meas} = \psi_{\rm orig} + \psi_{\rm ISM}, \tag{6}$$

where both $\psi_{\rm orig}$ and $\psi_{\rm ISM}$ are independent quantities that can vary from one sight line to the next.

Now for sight lines that intersect a stellar bubble, one must *subtract* the ISM contribution for that segment of the sight line passing through the bubble, which we signify as $\delta\psi_{\rm ISM}$. Then the contribution made by the bubble, $\psi_{\rm bub}$, must then be *added*. The total P.A. at Earth now becomes

$$\psi_{\rm meas} = \psi_{\rm orig} + \psi_{\rm ISM} - \delta\psi_{\rm ISM} + \psi_{\rm bub}. \tag{7}$$

The calculations in the following sections present maps specifically of $\psi_{\rm bub}$. Section 3 deals with the fact that the bubble contribution alone is not what is actually measured.

2.1. Azimuthal Fields

Modeling the P.A. morphologies of stellar bubbles requires the introduction of two coordinate systems: the observer system and the stellar one. For the observer Cartesian, cylindrical, and spherical coordinates are adopted as (x, y, z), (ϖ, α, z), and (r, θ, α), where the origin is the bubble center. Here z is the observer axis, with Earth at $+\infty$. The angle α is measured counterclockwise about this z-axis. Then θ is the polar angle from the observer axis. As we will be discussing sight lines intersecting the stellar bubble, the cylindrical radius ϖ will be the impact parameter for such rays. For the star, the corresponding Cartesian and spherical coordinates are (x_*, y_*, z_*) and (r, ϑ, φ).

For the transformation between these coordinates, we choose $y = y_*$. Using unit vectors, the viewing inclination angle i between the z and z_* axes is given by

$$\cos i = \hat{z} \cdot \hat{z_*}. \tag{8}$$

Transformations between the angular quantities can be obtained with spherical trigonometric relations, that will be used as needed.

In this first example, an azimuthal stellar magnetic field is considered. The vector field is $\boldsymbol{B} = B_\varphi\,\hat{\varphi}$. Calculation of Faraday rotation along a sight line requires determination of the LOS field component, which is given by

$$B_\parallel = \boldsymbol{B} \cdot \hat{z} = B_\varphi\,(\hat{\varphi} \cdot \hat{z}). \tag{9}$$

The transformation between the observer and stellar coordinates is needed to evaluate the preceding dot product; the rotation matrix between coordinate systems is given by

$$\begin{pmatrix} \hat{x_*} \\ \hat{y_*} \\ \hat{z_*} \end{pmatrix} = \begin{pmatrix} \cos i & 0 & \sin i \\ 0 & 1 & 0 \\ -\sin i & 0 & \cos i \end{pmatrix} \begin{pmatrix} \hat{x} \\ \hat{y} \\ \hat{z} \end{pmatrix}. \tag{10}$$

Consequently, one obtains

$$B_\parallel = -B_\varphi\,\sin\varphi\,\sin i. \tag{11}$$

In addition to the LOS field component, the distribution of the field strength with location about the star is also needed. We adopt the kinematic prescription put forth in Ignace et al. (1998) based on wind compression theory (Bjorkman & Cassinelli 1993). The Ignace et al. model assumes a magnetic field that is dynamically negligible as compared to the wind flow. Assuming flux freezing, the axisymmetric field topology can be derived, a result they refer to as "WCFields." Their model includes a parameter for the axisymmetric density distribution. For our purposes this parameter, $d\mu/d\mu_0$, is set to unity for a spherical wind; then using their asymptotic formula (Equation (21) of Ignace et al. 1998), the azimuthal field becomes simply

$$B_\varphi(r, \vartheta) = B_{\rm eff}\,\frac{R_*}{r}\,\sin\vartheta, \tag{12}$$

where ϑ is the co-latitude on the star, signifying that the maximum toroidal field strength occurs at the rotational equator of the star; and for the model of Ignace et al., the conveniently defined effective surface field strength, $B_{\rm eff}$, depends on the actual surface field strength B_*, the stellar rotation speed $v_{\rm rot}$, and the wind terminal speed v_∞, with

$$B_{\rm eff} = B_*\left(\frac{v_{\rm rot}}{v_\infty}\right). \tag{13}$$

Calculation of the Faraday rotation proceeds from a sight line-dependent integration through the bubble, as given by

$$\psi_{\rm bub}(\varpi, \alpha) = \frac{\pi}{z_{\rm b}}\int\left[\frac{B_\varphi(r, \vartheta)}{B_{\rm eff}}\right]\left[\frac{n_{\rm e}(r)}{n_{\rm w}}\right](\hat{z} \cdot \hat{\varphi})\,dz, \tag{14}$$

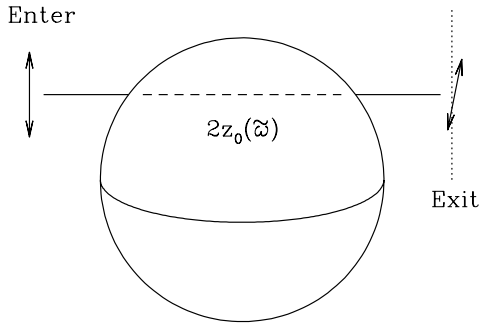

Figure 1. Illustration of the geometry for evaluating P.A. changes across spherical bubbles because of Faraday rotation. The observer is located off to the right. Linearly polarized radiation moving left to right passes through the bubble. Along an arbitrary sight line of impact parameter ϖ, the path length through the bubble will be given by $z_0 - (-z_0) = 2z_0 = 2\sqrt{R^2 - \varpi^2}$, where R is the radius of the bubble. Upon emerging, the orientation of the linear polarization against the sky will have rotated in a manner that depends on the magnetic field and electron density along the path.

with $n_e = n_w\,(R_*/r)^2$, where n_w is a density scale associated with the wind. This integral reduces to

$$\psi_{bub}(\varpi, \alpha) = -\frac{\pi}{z_b} \int \left(\frac{R_*}{r}\right)^3 \sin\vartheta\ \sin\varphi\ \sin i\, dz. \quad (15)$$

Note that $\sin\vartheta\,\sin\varphi \equiv y_*/r = y/r$ for our coordinate system definitions. Given that $y \perp z$, the coordinate y can be factored out of the integral, which now becomes

$$\psi_{bub}(\varpi, \alpha) = -\pi\ \sin i\ \frac{y}{z_b} \int \left(\frac{R_*}{r}\right)^4 \frac{dz}{R_*}. \quad (16)$$

To solve this equation, we note that $r^2 = \varpi^2 + z^2$, where ϖ is the impact parameter of the sight line under consideration, and therefore a constant of the integration. The sight line enters the bubble at $+z_0$ and exits at $-z_0$, where $z_0(\varpi) = \sqrt{R^2 - \varpi^2}$ (see Figure 1). Back-front symmetry of the integration gives

$$\psi_{bub}(\varpi, \alpha) = -2\pi\ \sin i\ \frac{y}{z_b} \int_0^{z_0(\varpi)} \left(\frac{R_*^2}{\varpi^2 + z^2}\right)^2 \frac{dz}{R_*}, \quad (17)$$

which, after some rearrangement, has the solution

$$\psi_{bub}(x, y) = -2\pi \left(\frac{R_*}{z_b}\right)\left(\frac{y}{\varpi}\right)\left(\frac{R_*}{\varpi}\right)^2 \sin i \times \left[(\pi/4 - \theta_0/2) + \frac{1}{4}\sin 2\theta_0\right], \quad (18)$$

where $\tan\theta_0 = \varpi/z_0(\varpi)$ and $\varpi = \sqrt{x^2 + y^2}$.

There are several key comments to be made about this solution.

1. First, the appearance of the factor of y means that the P.A. map is left–right *antisymmetric* about the line of $x = 0$ in the plane of the sky.
2. Second, the overall morphology of the P.A. map is *independent* of viewing inclination. The inclination angle appears in the solution only in the multiplicative factor $\sin i$, acting as an amplitude scale. Consequently, the P.A. map for the edge-on view is the same map that results for any other inclination, just the amount of P.A. rotation is reduced for every sight line by $\sin i$.

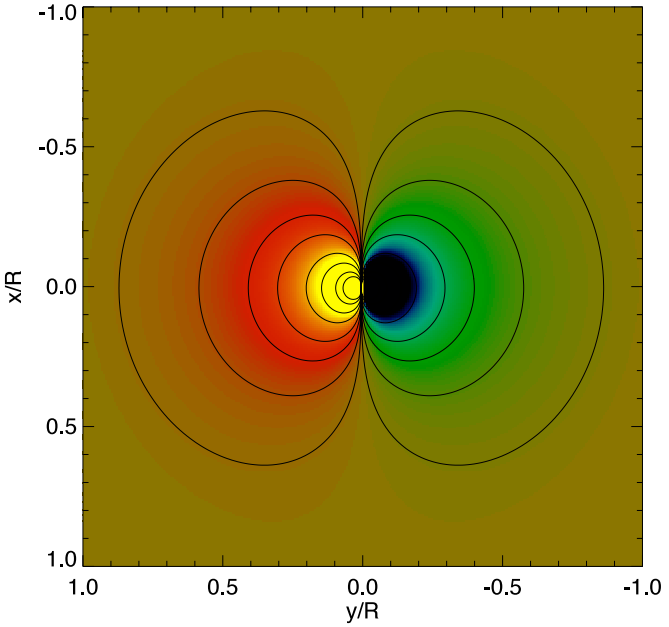

Figure 2. False color image with contours overlaid indicating the amplitude of the P.A. changes that would be observed across a wind-blown bubble with an azimuthal magnetic field. The plot is for the bubble contribution only. The green and blue colors are negative P.A. rotations; yellow and red are for positive values. The plot space is for the plane of the sky as y vs. x, with the coordinates normalized to the radius of the bubble R. Note the antisymmetric morphology, and that P.A. $= 0°$ along the $y = 0$ axis. Further, this morphology is valid for *all* viewing inclinations, with the amplitude of the P.A. rotation scaling linearly with $\sin i$.

(A color version of this figure is available in the online journal.)

Figure 2 shows a false-color plot of the P.A. map (or after proper normalization, the RM map) for the solution of Equation (18). Based on our conventions, the positive x-axis points down in this figure, and the positive y-axis points right; together these give positive z toward the observer. The map is indeed left–right antisymmetric and top–down symmetric. Additionally, because the azimuthal field is everywhere perpendicular to the LOS for $x = 0$, $\psi_{bub} = 0$ along the vertical that passes through the map center.

No absolute scale is given in this figure as it depends on a number of wind and star parameters, such as the surface field strength, the mass-loss rate, wind speed, and stellar radius as well as the bubble radius (hence, its age). We return to the expected level of P.A. and applications in Section 3.

2.2. Split Monopole Fields

It is useful to consider a different field topology to explore the range of P.A. map morphologies that can result in stellar bubbles. An azimuthal field exhibits the most shallow radial decline expected for a field that is carried out by a stellar wind. The next most shallow decline would be a split monopole. This is a radial magnetic field with a field strength $B_r = B_*\,(R_*/r)^2$, but the polarity changes sign from one hemisphere to the other. So the field is outward directed in one hemisphere, but inward in the other. Such a magnetic configuration is what would be expected of a strong stellar wind that distorts a dipole field at the star into a radial geometry (e.g., ud-Doula & Owocki 2002).

Calculation of P.A. maps proceeds as before, except that now there are different factors appearing in the integrand because of the new field topology. Instead of $\hat{z}\cdot\hat{\varphi}$ for the azimuthal field case, we now have $\hat{z}\cdot\hat{r} = z/r$ for a radial field. The integral

takes on the form:

$$\psi_{\rm bub} = -\frac{\pi}{z_{\rm bub}} \int \left[\frac{n_{\rm e}(r)}{n_{\rm w}}\right]\left[\frac{B_{\rm r}(r)}{B_*}\right]\left(\frac{z}{r}\right) dz. \quad (19)$$

Before proceeding, the split monopole case offers a new wrinkle for the calculation of the Faraday rotation. The radial field switches polarity between hemispheres. Consequently, at a general viewing inclination, the net Faraday rotation cancels identically for sight lines that do *not* intercept the magnetic equator. Such sight lines enter and exit the bubble in a hemispherical cap of just one field polarity. As a result, there is as much clockwise P.A. rotation through, say, the first half of the path length as there is counterclockwise contribution through the second half. The radial field ensures that for every value of $B_\parallel$ along the path, there is a corresponding value of $-B_\parallel$ at a reflected position in a back-front sense along the path. These two positions of opposed LOS field components occur at the same radius from the star, and therefore occur at the same density. A polarity switch, and therefore a net Faraday rotation, only occurs for sight lines that intercept the magnetic equator.

The result of all this is that a pair of truncated hemispherical caps appear at top and bottom in the P.A. maps for the split monopole case. The extent of these truncations depends on the viewing inclination. For the pole-on case, every sight line passes through the magnetic equator, and there are no truncation zones. The extreme opposite case is the edge-on view; here, no sight lines pass through the magnetic equator, and so $\psi_{\rm bub}$ is identically zero everywhere. In observer coordinates, the truncation occurs for $x \geqslant \pm R\cos i$.

For sight lines that do intercept the magnetic equator, the location along the path where this occurs, $z_{\rm eq}$, must be known so that the sign change is properly taken account in the integration. For sight lines with $|x| < R\cos i$, the integral becomes

$$\psi_{\rm bub} = -\frac{\pi}{z_{\rm b}} R_*^4 \left\{\int_{z_{\rm eq}}^{+z_0(\varpi)} \frac{z}{r^5}\, dz - \int_{-z_0(\varpi)}^{z_{\rm eq}} \frac{z}{r^5}\, dz\right\}, \quad (20)$$

where a sight line with impact parameter ϖ at observer azimuth α for a split monopole viewed at inclination i will intercept the equatorial plane at location

$$z_{\rm eq} = -\varpi\, \tan i\, \cos\alpha. \quad (21)$$

Evaluating the integral of Equation (20), along with some algebraic manipulation, leads to

$$\psi_{\rm bub} = -\frac{2\pi}{3}\left(\frac{R_*}{z_{\rm b}}\right)\left(\frac{R_*}{R}\right)^2\left[\left(\frac{R^2\,\cos^2 i}{x^2 + y^2\cos^2 i}\right) - 1\right]. \quad (22)$$

This solution is displayed in Figure 3 at a viewing inclination angle of $i = 60^\circ$.

Unlike the case of an azimuthal field, the scaling of the results for the P.A. is more complicated with viewing inclination. The truncated caps are inclination dependent. The P.A. maps for a split monopole are markedly different from that of an azimuthal field as seen in Figure 2. Whereas the azimuthal field produces an antisymmetric morphology, all the Faraday rotations for a split monopole are of the same sense: either everywhere clockwise or everywhere counterclockwise.

As noted previously, the effects of Faraday rotation are much smaller across the bubble for a split monopole than for an azimuthal field. However, assuming that $\psi_{\rm bub} \approx 0$ for the vast majority of sight lines in the split monopole case, the bubble still influences the P.A. map of the region because of differential RM effects for sight lines intercepting the bubble versus those that do not. In other words even if $\psi_{\rm bub} \ll 1$, the mere presence of the bubble means that $\delta\psi_{\rm ISM}$ may still be significant. More will be said about this in Section 3.

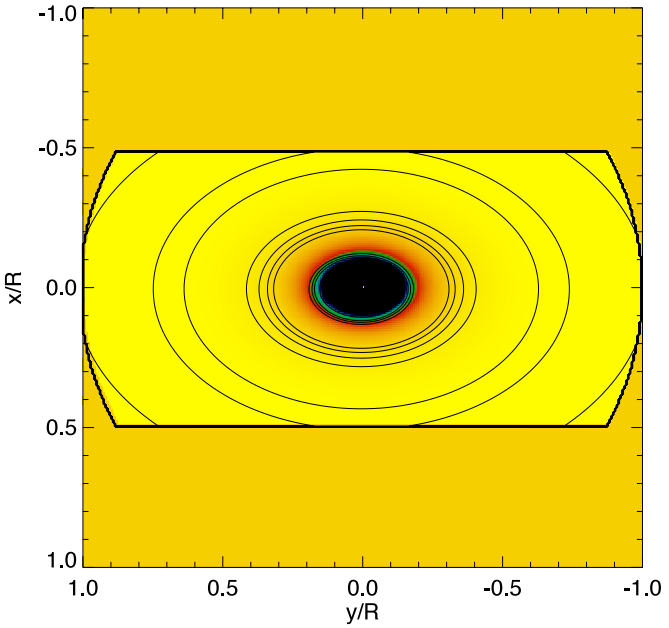

Figure 3. Similar to Figure 2, this P.A. map is for a split monopole field. In contrast to the azimuthal field case, the P.A. rotations are all of the same sense, either clockwise or counterclockwise (depending on the polarity of the field axis directed toward the observer). Sight lines that fail to intercept the magnetic equator when $|x| > R\cos i$ (see the text) make no contribution to a net Faraday rotation, leading to the appearance of "truncated" hemispheres; the example shown is for $i = 60^\circ$.

(A color version of this figure is available in the online journal.)

2.3. "Swept-up" Fields

For the last application, consider again the azimuthal field case. To simulate a two-wind interaction, where an inner wind (or a supernova ejecta shell) is blown into, and sweeps up, an outer wind from an earlier stage of stellar evolution, we impose a central spherical region that does not contribute to Faraday rotation. This could be either because the central region has no magnetic field or because it consists of neutral gas (the latter being unlikely for applications to massive stars). The overall scenario is intended to approximate situations like the production of a PN, or a fast wind from a blue supergiant overtaking a slower denser red giant wind (e.g., Chita et al. 2008), or an SN explosion that expands into the wind of a progenitor phase.

To be specific, we define an interior boundary of radius $R_1 < R_2$, now with R_2 the outer bubble radius. For $r < R_1$, the region is effectively a "cavity" in terms of its contribution to the Faraday rotation along a sight line. The polarization P.A., $\psi_{\rm bub}$, now becomes

$$\psi_{\rm bub} \propto y\, \sin i \times \int_{z_1}^{z_2} dz/r^3, \quad (23)$$

where $z_1 = 0$ for $\varpi \geqslant R_1$, but for $\varpi < R_1$, z_1 takes on the value

$$z_1 = \sqrt{R_1^2 - \varpi^2}. \quad (24)$$

Detailed steps for the derivation of $\psi_{\rm bub}$ as a function of sight line, along with a generalization to a power-law density, are given in the Appendix. Figure 4 shows examples of the resulting P.A. maps for cavities of different relative extents with $R_1/R_2 = 0.25$, 0.5, and 0.75. The maps remain left–right antisymmetric as in Section 2.1, but now two maxima appear in the form of arcs.

Not surprisingly, these maps are quite reminiscent of the morphologies seen in SNR G296.5+10.0 (Harvey-Smith et al. 2010). In that report, a discussion and derivation similar to this paper are presented. Harvey-Smith et al. introduced a toroidal field to explain the antisymmetric dependence of RM observed in the SNR. Those authors additionally included density and magnetic field enhancements arising from a shock. These are additional relevant ingredients that we have not incorporated here, but such effects could be included either in a phenomenological way or using detailed dynamical simulations. Our approach highlights the robust nature of the antisymmetric P.A. map morphology provided by an azimuthal field along with the appearance of arc-like features arising from the presence of a "cavity," a region devoid of any contribution to Faraday rotation.

3. DISCUSSION

The objective of this paper has been to elucidate the effects of Faraday rotation through a stellar bubble by evaluating of P.A. maps (or equivalently RM maps) under certain simplifying assumptions to focus on broad morphological trends. As such, spherical symmetry has been assumed for the geometry of the bubble and the run of density, specifically a wind-type density that drops as r^{-2} with radius. At this point it is worth commenting on the limitations of this approach, the kinds of effects that need to be included for application to particular types of bubbles, and strategies for best extracting information about the properties of the bubble and its immediate environment.

The case of an azimuthal stellar magnetic field is likely the only one of observational relevance because of its more gradual decline in field strength as r^{-1} to allow for detection at the 1–10 pc scale of stellar bubbles. A robust prediction of even the simplified models presented here is that a sign reversal in polarization P.A. (or RM) is expected when an azimuthal field plays a role in the Faraday rotation. However, that sign reversal will only be achieved if the $\psi_{\rm bub}$ term can be isolated.

Imagine a situation in which the ISM along a sight line passing near to a bubble, but without intercepting the bubble, produces a P.A. value of the form

$$\psi_{\rm ISM} = \pi \times L_0/z_{\rm ISM}, \tag{25}$$

where L_0 is the relevant length scale over which one can define an average product of the interstellar magnetic field and electron number density. In other words,

$$\langle B_\parallel n_{\rm e}\rangle = \frac{1}{L_0}\int_0^{L_0} B_\parallel n_{\rm e}\, dz. \tag{26}$$

Assuming that this average value is what would have been sampled for a sight line through the bubble, and further assuming spherical symmetry, the decrement to the interstellar P.A. rotation caused by the presence of the bubble as a function of impact parameter is

$$\delta\psi_{\rm ISM}(\varpi) = \psi_{\rm ISM}\,\frac{2R}{L_0}\sqrt{1-\frac{\varpi^2}{R^2}}. \tag{27}$$

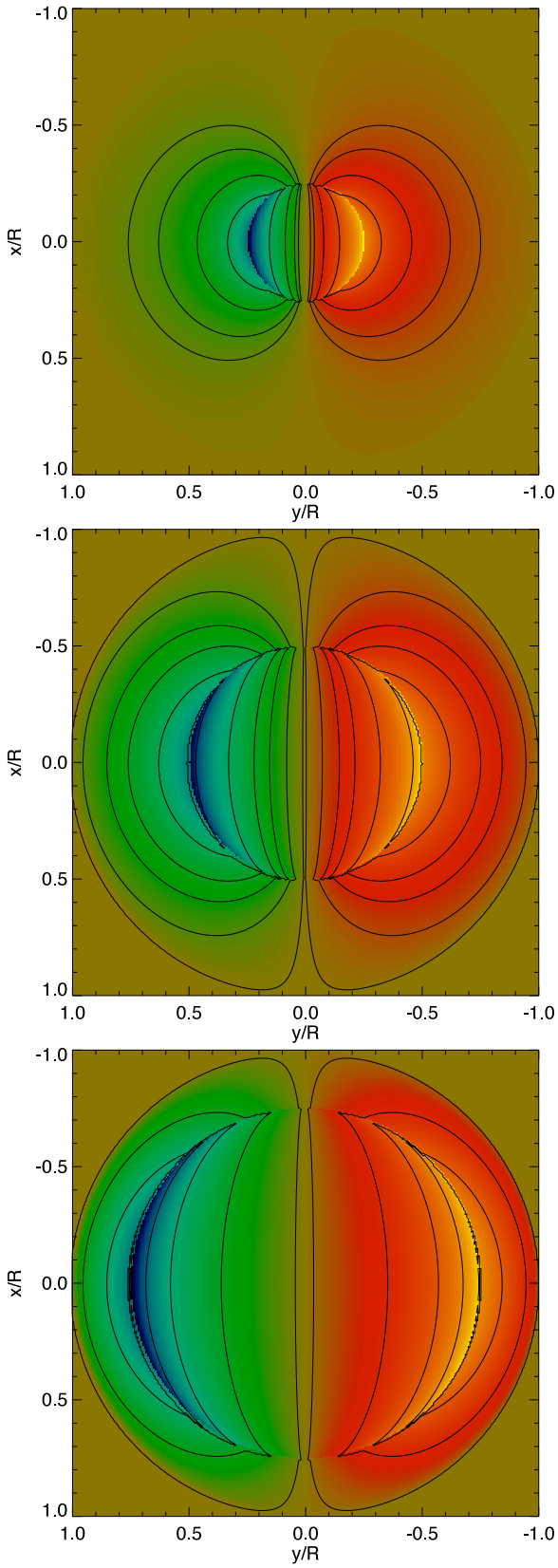

Figure 4. These three panels are for the case of an azimuthal field, now with an interior spherical region free of any magnetic field included. The intent is to approximate a two-wind interaction, with an inner, unmagnetized fast wind catching up to an outer slower and magnetized wind. The panels, from top to bottom, are for interior field-free regions with radii of 25%, 50%, and 75% of the bubble radius.

(A color version of this figure is available in the online journal.)

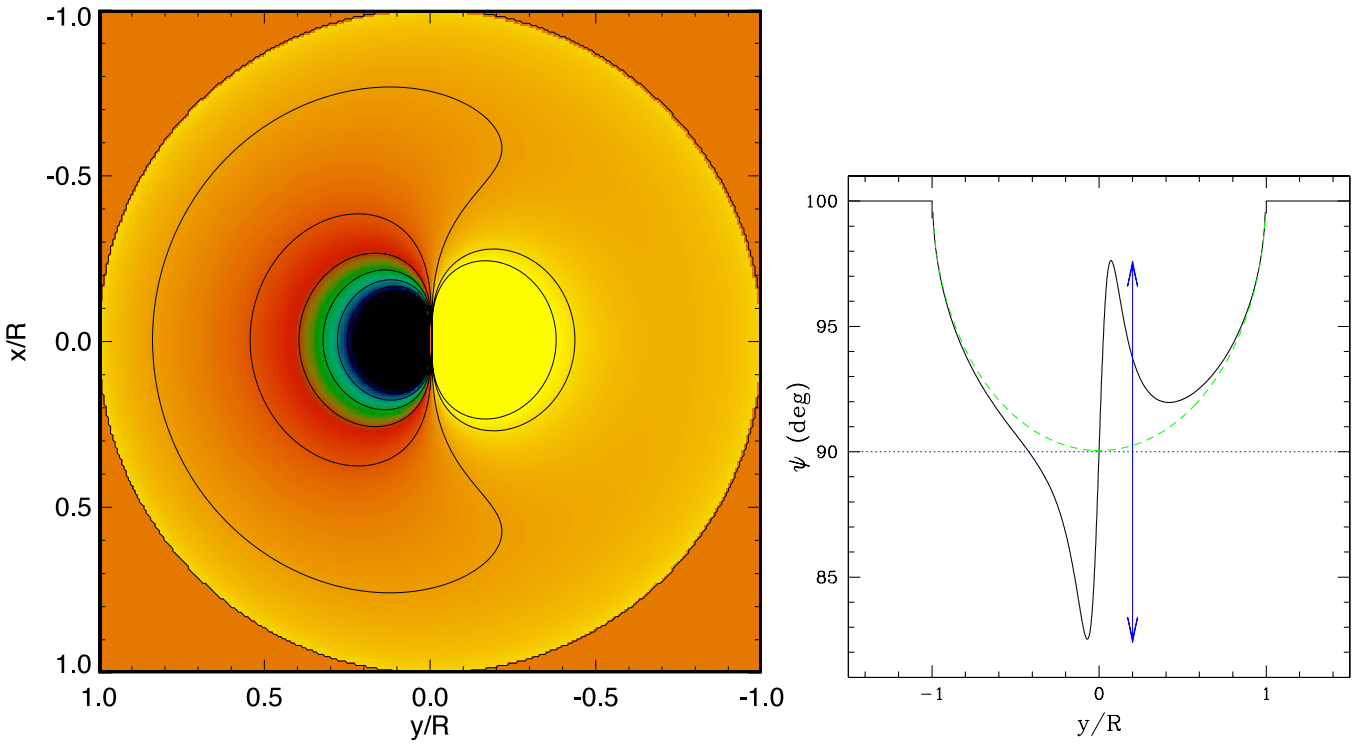

Figure 5. Panel (a) shows a P.A. map for a bubble with an azimuthal field, like Figure 3, but now with interstellar polarization effect included (see the text). Panel (b) shows how the polarization P.A. changes as a function of y along a horizontal line with $x = 0.1R$. Black is the full profile. Green signifies the term $\delta\psi_{\rm ISM}$. The horizontal blue line is the half-point between the two local maxima. Then the vertical blue arrows represent the full change in P.A. from one side of the bubble to the other because of $\psi_{\rm bub}(x, y)$.

(A color version of this figure is available in the online journal.)

The ISM is highly inhomogeneous in terms of its magnetic field distribution, density, and ionization. Consequently, one hardly expects that $n_{\rm e} B_\parallel$ at the location of the wind bubble would equal the path-length-averaged value $\langle B_\parallel\, n_{\rm e}\rangle$. Still, it is useful to consider the resultant P.A. map from the combination of the different contributions by adopting such a scenario. Choosing $\psi_{\rm ISM}$[3] $= 1000^\circ$ and $2R/L_0 = 0.01$, Figure 5(a) shows a P.A. map and contours for an azimuthal field case, similar to the style of previous figures, but now with the Faraday rotation contribution from the ISM included. Additionally, Figure 5(b) displays what the measured P.A. would be along an axis at $x = 0.1R$.

Figure 5 is important for illustrating how to infer the various components to the measured value of $\psi_{\rm meas}$. If one could measure the P.A. map across a wind-blown bubble with an azimuthal field, the following outlines how to decompose the trace of the signal in Figure 5(b) to determine $\psi_{\rm ISM}$, $\delta\psi_{\rm ISM}$, and $\psi_{\rm bub}$. Note that it is assumed that the interstellar field and electron density in the vicinity of the bubble is approximately constant (or at least smoothly varying).

1. For $|y| > R$, the P.A. is set by sight lines that do not intercept the bubble and therefore sample the interstellar field and electron density.
2. For $|y| < R$, the sight lines intercept the bubble. The azimuthal field leads to $\psi_{\rm bub}$ that is predicted to be antisymmetric, but the decrement term $\delta\psi_{\rm ISM}$ is symmetric. The result is a left–right asymmetric profile.
3. The two peaks in Figure 5(b) can be used to deduce the amplitude of $\psi_{\rm bub}$. The vertical blue double-arrowed line represents the total change in the P.A. rotation owing to the bubble contribution. Introducing $\psi_{\rm max}(x) = |\psi_{\rm bub}(x, y_{\rm max})|$ as being the maximum P.A. rotation through the bubble at location $(x, \pm y_{\rm max})$, the blue arrow has an amplitude of $2\psi_{\rm max}$. The value of $\psi_{\rm max}$ is related to the scale length $z_{\rm b}$ that depends on the wavelength of observation, the density scale of the bubble, and importantly the surface field strength of the star. Bisection of the vertical arrow, as illustrated with the horizontal dotted line, yields the value of $\psi_{\rm max}$.
4. The bisection mentioned in the previous point gives the maximum decrement due to $\delta\psi_{\rm ISM}$. With spherical symmetry, one should expect a distribution of this decrement as indicated by the green dashed line. Bear in mind that the particular example of Figure 5 implicitly assumes a local interstellar field of positive polarity, which leads to the bowl-shaped decrement as shown. If the local field were of the opposite polarity, the "decrement" would in fact produce an *inverted* bowl shape, meaning that the green line for $\delta\psi_{\rm ISM}$ would lie above $\psi_{\rm ISM}$. Consequently, the decomposition process gives both the strength of the local magnetic field and its polarity. As one last comment, it is possible that no decrement is found. Such a result would arise if the interstellar field in the locale of the bubble were very low, or if the local ISM were of low ionization.

To be yet more quantitative, it is possible to relate a measured value of $\psi_{\rm max}$ from the bubble contribution to the length scale $z_{\rm b}$. Equation (18) gives the solution for $\psi_{\rm bub}$ in the azimuthal field case. Figure 6 plots the value of $|y_{\rm max}|$ as a function of x. In other words, holding x fixed and measuring the polarization P.A. in a direction perpendicular to the axis of antisymmetry, Figure 6 provides the location $(x, y_{\rm max})$.

[3] Recall that polarization P.A. is degenerate in multiples of 180°; here $\psi_{\rm ISM} = 1000^\circ$ amounts to a P.A. of 100°, as seen in Figure 5(b).

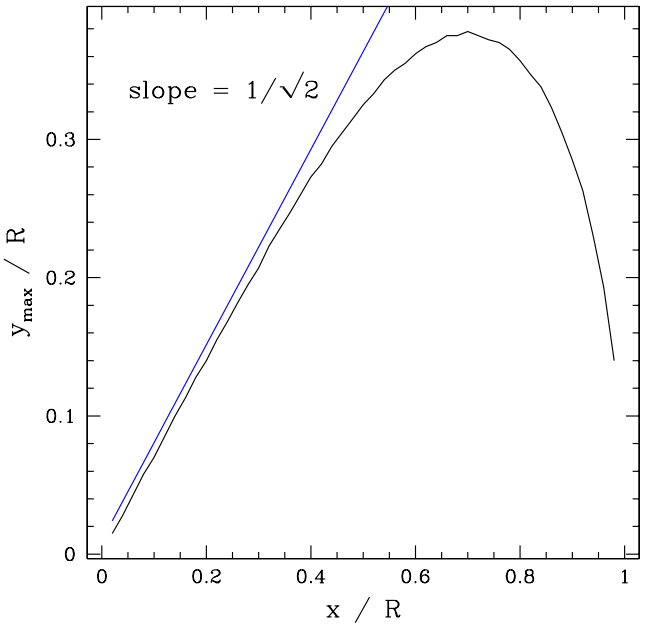

Figure 6. Solution for the location of $y_{\max}(x)$, where $\psi_{\max}$ is achieved in the case of a wind-blown bubble with an azimuthal magnetic field (but no cavity). The black line is the numerical solution. For $x/R \ll 1$, $y_{\max}/R$ is also small, indicating that $\psi_{\max}$ occurs near the projected center of the bubble. In this limit $y_{\max} \approx x/\sqrt{2}$, as shown by the blue line, which has the correct slope but is shifted upward slightly for ease of viewing.

(A color version of this figure is available in the online journal.)

The scaling for the P.A. rotation increases rapidly with decreasing value of the impact parameter, ϖ. Consequently, the strongest measurable effect of the bubble for Faraday rotation will be around the center of the projected bubble. At these locations, one has $\theta_0 \approx 0$, for which $y_{\max}$ is easily derived to be

$$y_{\max} \approx x/\sqrt{2}, \tag{28}$$

which is indicated by the blue line in Figure 6. The value of $\psi_{\max}$ is also straightforwardly derivable as

$$\psi_{\max} \approx \sqrt{\frac{1}{27}}\,\pi^2\,\sin i\,\left(\frac{R_*^3}{z_{\rm b}\,x^2}\right), \tag{29}$$

where $\psi_{\max}$[4] is measured from the data corresponding to a selection of x on the P.A. map. From these measures one can determine $z_{\rm b}/\sin i$ from the data. In the absence of any other information, there is an inclination ambiguity. Still, an upper limit to $z_{\rm b}$ is obtained from assuming an edge-on view of the system, in which case a lower limit to the stellar surface magnetic field strength is also obtained.

The overall scale of the P.A. rotation through a stellar bubble is set by a combination of stellar and wind parameters, and the size of the bubble itself (which, of course, is related to its age). For the azimuthal field case, which is the one most likely to be of observational significance, we have already that $B_\varphi = B_{\rm eff}\,(R_*/r)$. For the number density of electrons in a spherical stellar wind, we have been using $n_{\rm e} = n_{\rm w}\,(R_*/r)^2$. The density scale constant is given by

$$n_{\rm w} = \frac{\dot{M}}{4\pi\,\mu_{\rm e} m_H\,v_\infty\,R_*^2}, \tag{30}$$

where $\dot{M}$ is the mass-loss rate, $\mu_{\rm e}$ is the mean molecular weight per free electron, and v_∞ is the wind terminal speed. Then, the scale constant for Faraday rotation becomes

$$\psi_0 = 6\overset{\circ}{.}0 \times \frac{\left(\frac{B_{\rm eff}}{10\,{\rm G}}\right)\left(\frac{R_*}{100\,R_\odot}\right)\left(\frac{\dot{M}/\mu_{\rm e}}{10^{-6}\,M_\odot\,{\rm yr}^{-1}}\right)}{\left(\frac{v_\infty}{100\,{\rm km\,s}^{-1}}\right)\left(\frac{R}{1\,{\rm pc}}\right)^2} \times \left(\frac{\lambda}{30\,{\rm cm}}\right)^2. \tag{31}$$

This scale parameter is found to be larger for stars with stronger surface fields, larger size, and higher mass-loss winds; it is smaller for faster winds and larger (older) bubbles. It also has the standard quadratic dependence on wavelength.

Using the preceding expressions, one can derive a ratio of the stellar radius to the Faraday rotation length scale for the bubble, $z_{\rm b}$, to be

$$\frac{R_*}{z_{\rm b}} = 4 \times 10^{11} \times \frac{\left(\frac{B_{\rm eff}}{10\,{\rm G}}\right)\left(\frac{\dot{M}/\mu_{\rm e}}{10^{-6}\,M_\odot\,{\rm yr}^{-1}}\right)}{\left(\frac{v_\infty}{100\,{\rm km\,s}^{-1}}\right)\left(\frac{R_*}{100 R_\odot}\right)} \times \left(\frac{\lambda}{30\,{\rm cm}}\right)^2. \tag{32}$$

The scale of this ratio is huge and thus warrants a comment of interpretation. Implicit is that the length scale for Faraday rotation $z_{\rm b}$ has been evaluated for the magnetic field and wind density near the stellar surface, which are enormous compared with interstellar conditions. As a result, $z_{\rm b}$ is driven to incredibly small values on the order of 1 cm and less. However, expected values of Faraday rotation across the bubble are much smaller than at the scale of the star. Defining an associated scale $z_{\rm b}'$ related to the dimensions of the bubble instead of the star gives $(R/z_{\rm b}') = (R_*/z_{\rm b}) \times (R_*/R)^2$, which when using the parameterization of Equation (32) is of order 10^{-2}. In other words, the length scale associated with rotation of the polarization P.A. through 180° is roughly 100 times larger than the radius of the bubble.

4. CONCLUSIONS

The goal of this study has been to develop insight into the possibilities of using Faraday rotation to probe stellar magnetism in wind-blown bubbles. Adopting spherical symmetry and considering two field topologies of azimuthal and split monopole fields, analytic and semianalytic results were presented in the form of P.A. maps arising from Faraday rotation across a stellar wind bubble. The field strength for a split monopole declines too fast to have detectable effects for Faraday rotation. Instead, only the azimuthal field scenario is likely to lead to detectable signals, for which the key result derived here is the antisymmetric morphology for the P.A. rotations (or equivalently, the RMs) across the bubble in addition to a simple $\sin i$ scaling of the amplitude of P.A. rotation. Inclusion of a central spherical

[4] The reader might be concerned that the value of $\psi_{\max}$ appears to diverge as $x \to 0$, for which $y_{\max} \to 0$ as well. First, the apparent divergence does not take place owing to the finite size of the star. Second, although large values of $\psi_{\max}$ can be achieved, the polarization P.A. suffers a 180° degeneracy. Many rotations in ψ over a small observed angular scale rapidly leads to polarimetric cancellation. For expected star, wind, and bubble parameters, the vast majority of the bubble will like have at best a modest value of ψ, except perhaps at quite long wavelengths.

region of zero magnetic field leads to prominent and antisymmetric P.A. rotations in arc-like structures like those observed in SNR G296.5+10.0 (Harvey-Smith et al. 2010).

To date, studies of Faraday rotation effects across HII regions appear consistent with variations in the interstellar magnetic field (e.g., Harvey-Smith et al. 2011). Clearly there may be only a restricted subset of bubbles for which our models will have applications. Moreover, dispersion in the interstellar RM may present challenges in detection and interpretation of the effects we have described even when present, as, for example, variations in the interstellar RM can have typical amplitudes of order 10 rad m^{-2} (Mao et al. 2010). We are considering strategies for interpreting the interaction of interstellar magnetic fields with stellar bubbles using Faraday rotation effects. Given recent results in relation to SNR G296.5+10.0, the PN cases (Ransom et al. 2008, 2010), and the Rosette Nebula (Savage et al. 2012), Faraday rotation offers great promise as a means of using stellar bubbles to discern the properties of stellar and/or interstellar magnetic fields.

The authors are grateful to Steve Gibson for many helpful discussions on astrophysical problems involving Faraday rotation and also to the anonymous referee for comments that have improved this paper. R.I. acknowledges support for this research through a grant from the National Science Foundation (AST-0807664). N.M.P. acknowledges support from the National Science Foundation Research Experiences for Undergraduates (REU) program through grant AST-1004872.

APPENDIX

GENERALIZED SOLUTION FOR A STELLAR WIND WITH AN AZIMUTHAL MAGNETIC FIELD

For an azimuthal magnetic field of the form $B_\varphi \propto 1/r$, there is a general solution to the P.A. distribution arising from Faraday rotation for a spherically symmetric envelope with an electron density that is a power law in radius, $n_e \propto r^{-m}$, with m being the power-law exponent. Consider a bubble of outer radius R_2 and inner radius R_1. For $r < R_1$, the interior region makes no contribution to the Faraday rotation. Using θ as the variable of integration, with $\tan\theta = \varpi/z$, a sight line enters the outer bubble edge at θ_2 and enters the inner region at θ_1. Then the solution for the P.A. rotation arising from the bubble contribution is

$$\psi_{\rm bub} = \pi \left(\frac{2R_2}{z_b}\right)\left(\frac{R_2}{\varpi}\right)^m \left(\frac{y}{\varpi}\right) \sin i \int_{\theta_2}^{\theta_1} \sin^m\theta \, d\theta. \quad \text{(A1)}$$

Although the preceding integral is mathematically valid, it may not be physically plausible for arbitrary values of m. The selection of $B_\varphi \propto r^{-1}$ essentially assumes a frozen-in field that is dragged out with the wind plasma in a constant expansion flow (e.g., Weber & Davis 1967), implying an inverse square-law density. However, $m \neq 2$ could represent changes in the ionization state of the gas with distance from the star.

The integration of Equation (A1) takes into account the front-back symmetry of the situation by integrating only over the front hemisphere facing the observer. This gives rise to the factor of two appearing in the first fraction. The integration limits also allow for an interior central cavity of zero field (or, alternatively, zero ionization) to the wind-blown bubble, as was discussed in the swept-up wind case of Section 2.3.

With or without a central cavity, the upper limit to the integral is always given by

$$\sin\theta_2 = \varpi/R_2, \quad \text{(A2)}$$

for a bubble of outer radius R_2. The presence of a cavity only affects the lower limit to the integral. If there is no cavity, then $\theta_1 = \pi/2$ for all sight lines. However, within an interior cavity of radius R_1, the lower limit of $\theta_1 = \pi/2$ holds only for sight lines that *fail* to intercept the cavity region, with $\varpi \geqslant R_1$. Sight lines with $\varpi < R_1$ pass through the cavity; the upper limit to the integration now becomes

$$\sin\theta_1 = \varpi/R_1. \quad \text{(A3)}$$

REFERENCES

Alecian, E., Kochukhov, O., Neiner, C., et al. 2011, A&A, 536, L6
Babcock, H. W. 1947, ApJ, 105, 105
Babel, J., & Montmerle, Th. 1997a, A&A, 323, 121
Babel, J., & Montmerle, Th. 1997b, ApJL, 485, L29
Beck, R. 2012, SSRv, 166, 215
Berdyugina, S. V., & Fluri, D. M. 2004, A&A, 417, 775
Bjorkman, J. E., & Cassinelli, J. P. 1993, ApJ, 409, 429
Blandford, R. D., & Payne, D. G. 1982, MNRAS, 199, 883
Bodenheimer, P. 1995, ARA&A, 33, 199
Bommier, V. 2012, A&A, 539, 122
Braithwaite, J. 2006, A&A, 449, 451
Brown, J. C., Cassinelli, J. P., & Maheswaran, M. 2008, ApJ, 688, 1320
Cantiello, M., Langer, N., Brott, I., et al. 2009, A&A, 499, 279
Carilli, C. L., & Taylor, G. B. 2002, ARA&A, 40, 319
Chevalier, R. A., & Luo, D. 1994, ApJ, 421, 225
Chita, S. M., Langer, N., van Marle, A. J., Garcia-Segura, G., & Heger, A. 2008, A&A, 488, L37
Davidson, K., & Ostriker, J. P. 1973, ApJ, 179, 585
de Becker, M., Rauw, G., Sana, H., et al. 2006, MNRAS, 371, 1280
Donati, J.-F., & Collier Cameron, A. 1997, MNRAS, 291, 1
Donati, J.-F., & Landstreet, J. D. 2009, ARA&A, 47, 333
Dougherty, S. M., & Williams, P. M. 2000, MNRAS, 319, 1005
Favata, F., Neiner, C., Testa, P., Hussain, G., & Sanz-Focada, J. 2009, A&A, 495, 217
Gagne, M., Caillault, J.-P., Stauffer, J. R., & Linsky, J. L. 1997, ApJL, 478, L87
Gagne, M., Fehon, G., Savoy, M. R., et al. 2011, ApJS, 194, 5
Gagne, M., Oksala, M. E., Cohen, D. H., et al. 2005, ApJ, 628, 986
Ghosh, P., & Lamb, F. K. 1979, ApJ, 234, 296
Grunhut, J. H., Rivinius, Th., Wade, G. A., et al. 2012a, MNRAS, 419, 1610
Grunhut, J. H., Wade, G. A., Sundqvist, J. O., et al. 2012b, MNRAS, 426, 2208
Grunhut, J. H., Wade, G. A., Leutenegger, M., et al. 2013, MNRAS, 428, 1686
Güdel, M., & Nazé, Y. 2009, A&ARv, 17, 309
Han, J. L., Manchester, R. N., Lyne, A. G., Qiao, G. J., & van Straten, W. 2006, ApJ, 642, 868
Harvey-Smith, L., Gaensler, B. M., Kothes, R., et al. 2010, ApJ, 712, 1157
Harvey-Smith, L., Madsen, G. J., & Gaensler, B. M. 2011, ApJ, 736, 83
Hubrig, S., Schöller, M., Kharchenko, N. V., et al. 2011, A&A, 528, 151
Hubrig, S., Schöller, M., Kholtygin, A. F., et al. 2012, A&A, 546, L6
Ignace, R., Cassinelli, J. P., & Bjorkman, J. E. 1998, ApJ, 505, 910
Ignace, R., Hole, K. T., Cassinelli, J. P., & Henson, G. D. 2011, A&A, 530, 82
Ignace, R., Nordsieck, K. H., & Cassinelli, J. P. 1997, ApJ, 486, 550
Ignace, R., Oskinova, L. M., Jardine, M., et al. 2010, ApJ, 721, 1412
Ignace, R., Oskinova, L. M., & Massa, D. 2013, MNRAS, 429, 516
Li, Q.-K., Cassinelli, J. P., Brown, J. C., Waldron, W. L., & Miller, N. A. 2008, ApJ, 672, 1174
Lopez Ariste, A., Asensio Ramos, A., & Gonzalez Fernandez, C. 2011, A&A, 527, 120
MacGregor, K. B., & Cassinelli, J. P. 2003, ApJ, 586, 480
Maeder, A., & Meynet, G. 2003, A&A, 411, 543
Manso Sainz, R., & Martinez Gonzalez, M. J. 2012, ApJ, 760, 7
Mao, S. A., Gaensler, B. M., Haverkorn, M., et al. 2010, ApJ, 714, 1170
Matt, S. P., MacGregor, K. B., Pinsonneault, M. H., & Greene, T. P. 2012, ApJL, 754, L26
McKee, C. F., & Ostriker, E. C. 2007, ARA&A, 45, 565
Meynet, G., Eggenberger, P., & Maeder, A. 2011, A&A, 525, L11

Minter, A. H., & Spangler, S. R. 1996, ApJ, 458, 194
Oskinova, L. M., Todt, H., Ignace, R., et al. 2011, MNRAS, 416, 1456
Petit, V., Massa, D. L., Marcolino, W. L. F., Wade, G. A., & Ignace, R. 2011, MNRAS, 412, L45
Poe, C. H., Friend, D. B., & Cassinelli, J. P. 1989, ApJ, 337, 888
Ransom, R. R., Kothes, R., Wolleben, M., & Landecker, T. L. 2010, ApJ, 724, 946
Ransom, R. R., Uyaniker, B., Kothes, R., & Landecker, T. L. 2008, ApJ, 684, 1009
Sahal-Brechot, S., Bommier, V., & Leroy, J. L. 1977, A&A, 59, 223
Savage, A. H., Spangler, S. R., & Fischer, P. D. 2012, arXiv:1206.5173
Schöller, M., Hubrig, S., Ilyin, I., et al. 2011, AN, 332, 994
Sennhauser, C., & Berdyugina, S. V. 2011, A&A, 529, 100
Shore, S. N., & Brown, D. N. 1990, ApJ, 365, 665
Stenflo, J. O. 1982, SoPh, 80, 209
Townsend, R. H. D., & Owocki, S. P. 2005, MNRAS, 357, 251
Townsend, R. H. D., Owocki, S. P., & ud-Doula, A. 2007, MNRAS, 382, 139
Trujillo Bueno, J., Merenda, L., Centeno, R., Collados, M., & Landi Degl'Innocenti, E. 2005, ApJL, 619, L191
ud-Doula, A., & Owocki, S. P. 2002, ApJ, 576, 413
ud-Doula, A., Owocki, S. P., & Townsend, R. H. D. 2008, MNRAS, 385, 97
ud-Doula, A., Sundqvist, J. O., Owocki, S. P., Petit, V., & Townsend, R. H. D. 2013, MNRAS, 428, 2723
van Loon, S., Runacres, M. C., & Blomme, R. 2006, A&A, 452, 1011
Wade, G. A., Alecian, E., Bohlender, D. A., et al. 2011, in IAU Symp. 272, Active OB Stars: Structure, Evolution, Mass Loss, and Critical Limits, ed. C. Neiner et al. (Cambridge: Cambridge Univ. Press), 118
Wade, G. A., Maiz Apellaniz, J., Martins, F., et al. 2012, MNRAS, 425, 1278
Weber, E. J., & Davis, L. 1967, ApJ, 148, 217
Williams, P. M., Dougherty, S. M., Davis, R. J., et al. 1997, MNRAS, 289, 10
Yoon, S.-C., Dierks, A., & Langer, N. 2012, A&A, 542, 113